

Non-Equilibrium Spark Plasma Reactive Doping Enables Highly Adjustable Metal to Insulator Transitions and Improved Mechanical Stability for VO₂

*Xuanchi Zhou^{a†}, Yuchen Cui^{a†}, Yanlong Shang^a, Haifan Li^a, Jiaou Wang^b, Ye Meng^c,
Xiaoguang Xu^a, Yong Jiang^{a*}, Nuofu Chen^{d*} and Jikun Chen^{a*}*

^a *School of Materials Science and Engineering, University of Science and Technology Beijing, Beijing, 100083, China*

^b *Beijing Synchrotron Radiation Facility, Institute of High Energy Physics, Chinese Academy of Sciences, Beijing 100049, China*

^c *Institute for Advanced Materials and Technology, University of Science and Technology Beijing, Beijing 100083, China*

^d *School of Renewable Energy, North China Electric Power University, Beijing 102206, China*

*Authors to whom correspondence should be addressed: jikunchen@ustb.edu.cn (J. Chen), yjiang@ustb.edu.cn (Y. Jiang), nfchen@ncepu.edu.cn (N. Chen).

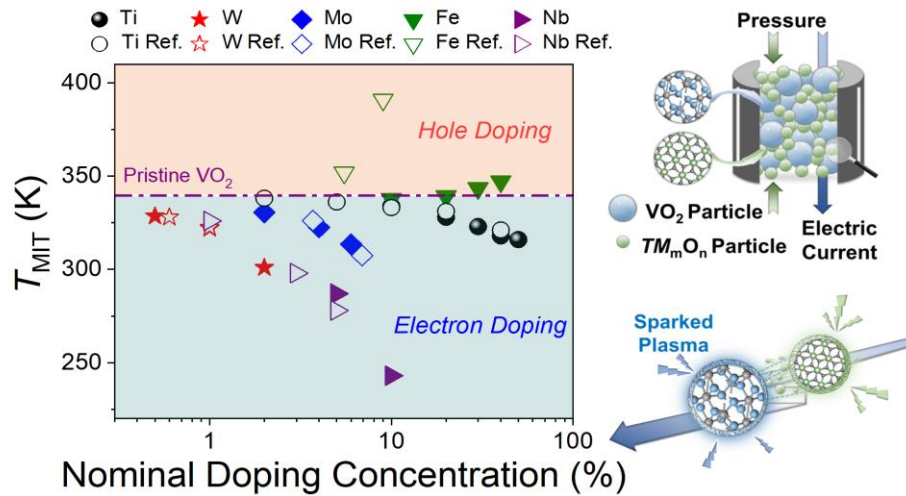
[†] X. Zhou and Y. Cui contributed equally to this work.

Abstract

Although vanadium dioxide (VO_2) exhibits the most abrupt metal to insulator transition (MIT) properties near room-temperature, the present regulation of their MIT functionalities is insufficient owing to the high complexity and susception associated with V^{4+} . Herein, we demonstrate a spark plasma assisted reactive sintering (SPARS) approach to simultaneously achieve *in situ* doping and sintering of VO_2 within largely short period (~ 10 minutes). This enables high convenience and flexibility in regulating the electronic structure of VO_2 via dopant elements covering Ti, W, Nb, Mo, Cr and Fe, leading to a wide adjustment in their metal to insulator transition temperature (T_{MIT}) and basic resistivity (ρ). Furthermore, the mechanical strengths of the doped- VO_2 were meanwhile largely improved via the compositing effect of high melting-point dopant oxide. The high adjustability in MIT properties and improved mechanical properties further paves the way towards practical applications of VO_2 in power electronics, thermochromism and infrared camouflage.

Key words: Quantum materials, Electronic phase transition, Correlated oxides, Correlated electronics;

TOC Graphic



1. Introduction

The metal to insulator transition (MIT) within *d*-band correlated oxides brings in abrupt changes in regulating their electronic and optical properties beyond conventional semiconductors¹⁻³. Among the existing family of MIT materials, the vanadium dioxide (VO₂) exhibits the most abrupt MIT properties near room-temperature that plays an irreplaceable role in applications, such as thermochromism⁴⁻⁶, infrared camouflage^{7,8}, and correlated electronic devices⁹⁻¹². Nevertheless, these applications of VO₂ are still challenged by its material synthesis as the electronic phase diagram of vanadium oxides is extraordinarily complex¹³. For example, the metal to insulator transition temperature (T_{MIT}) that triggers the MIT is known to be rather sensitive to the valence state of vanadium that is at the intermediate valence state (e.g., V⁴⁺) and susceptible to both oxidizing and reducing environment¹⁴⁻¹⁶. Conventionally, the MIT properties and electronic structure of VO₂ is adjusted by the elementary substitution, e.g., the T_{MIT} is elevated or descended via substituting V⁴⁺ by dopants with lower or higher valence states, respectively^{17,18}.

To achieve the abrupt variation in the material resistivity during the MIT of VO₂, it is vital to precisely control the concentration and homogeneity in the distribution of the dopant elements, without extrinsically altering the oxygen composition¹⁹. As compared to the vacuum deposition of doped-VO₂ thin films via plasmanized or vaporized precursors²⁰⁻²³, achieving a precise elementary substitution for the bulk materials of VO₂ while maintaining their MIT abruptness is more difficult. Previously, doped VO₂ bulk pellets were made using the following two routes: 1) Firstly synthesizing the powder materials for doped VO₂, and afterwards sintering such powder into bulk pellets at precisely controlled atmosphere^{24,25}. 2) Co-sintering VO₂ and dopant oxides at high temperatures over a long period (e.g., several days) at controlled atmosphere²¹. Usually, the homogeneity and achievable concentration of the dopant element within VO₂ are restricted by its equilibrium phase diagram, while the kinetic process that triggers the diffusion of the dopant elements may easily disturb the desired valence state of vanadium^{26,27}. Up to date, an effective strategy to accurately adjust the MIT properties of the VO₂ bulk material via conveniently achievable elementary substitution is yet lacking, and this impedes applying VO₂ for power electronics as discrete elementary devices.

In this article, we demonstrate a spark plasma assisted reactive sintering (SPARS) strategy that largely elevates the flexibility and effectiveness in the elementary substitution of VO₂ as bulk material, covering a large abundance of the dopant elements such as Ti, W, Nb, Mo, Cr, and Fe. The non-equilibrium process related to SPARS largely shortens the diffusion period of the dopants (e.g., 10 minutes), and it enables a broad adjustment of the electronic structure and the MIT functionality of VO₂. Compliant variations in the electronic structure of VO₂ were probed via the near-edge X-ray absorption fine structure (NEXAFS) analysis that differs from the conventional doping of semiconductors. Furthermore, the unreacted dopant oxides

with high melting point can be meanwhile used to improve the mechanical properties of VO₂, paving the way towards their practical applications in power electronics.

2. Experimental Section

A spark plasma assisted reactive sintering (SPARS) strategy was used for synthesizing the doped VO₂ bulk materials. The as-proposed SPARS approach includes the following two steps. In the first step, the powder of VO₂ is homogeneously mixed with the transition metal oxides (TM_mO_n) dopants at the desired stoichiometry, and afterwards pressed inside a graphite die. In the second step, a large electric current (e.g., 300 A/cm²) and high pressure (e.g., 20 MPa) are imparted into the graphite die and trigger the solid-state reaction between VO₂ and TM_mO_n powders at the temperature of 900 °C for 10 minutes under a vacuum atmosphere. The as-made VO₂ bulk material was a pellet with the radius of 10 mm and the thickness of around 4 mm.

The crystal structure of samples was characterized by the X-ray diffraction (XRD) (RIGAKU, Smartlab). The valence state of as-made samples was characterized by X-ray photoelectron spectroscopy (XPS) (Kratos, AXIS ULTRA^{DLD}) that was equipped with monochromatic Al-K α source (150 W) and photon energy of 1486.6 eV. All the binding energies as obtained from the XPS were referenced to the C 1s peak from the adventitious carbon at 284.8 eV, while a Shirley function was used to subtract the background. **In addition, the valence state of vanadium for VO₂ is indicated by the binding energy of V 2p_{3/2} and V 2p_{1/2} peaks. To fit the XPS curves, the V 2p_{3/2} peak can be resolved by the two binding energies at 516.3 and 515.7 eV that represents the valence state of V⁴⁺ and V³⁺, respectively. The V 2p_{1/2} region can be analogously divided into the two peaks that are respectively located at 523.6 and 523.0 eV, according to the previous reports^{28, 29}.** And their morphologies were characterized by scanning electron microscopy (SEM) and energy dispersion spectrum (EDS). The electronic structures of as-made samples were also investigated by the near edge X-ray absorption fine structure (NEXAFS). To characterize their electrical transportation properties, their temperature dependences of resistivity within 300-400 K were measured by using a commercialized CTA-system in vacuum, while the one within 1.8-400 K was measured by using the physical property measurement system (PPMS) (Quantum Design). The Vickers hardness of VO₂ bulk material were measured by the digital Vickers hardness tester (VTD 512) at room-temperature under the load of 500 kgf.

3. Results and Discussion

3.1. Strategy for elementary substitution of VO₂ via SPARS

To address the center challenge in the precise element doping for bulk VO₂, herein a spark plasma assisted *in situ* doping strategy is used, as illustrated in Fig. 1a. Unlike the previous literatures that uses the reactive spark plasma process for sintering the powder material into bulk pellet, or directly synthesizing compounds from their respective elementary substances^{30, 31}, herein the reactive spark plasma is

used to achieve the element doping of oxides. Firstly, the powder of VO₂ is homogeneously mixed with the doped transitional metal oxides (TM_mO_n , $TM = Ti, W, Nb, Mo, Fe, \text{ and } Cr$) and pressed inside a graphite die. Afterwards, a large DC electric current (e.g., around 300 A/cm²) and high pressure (e.g., 20 MPa) are imparted to spark over the powder precursor that triggers their mutual element diffusion and rapidly elevate the temperature to 900 °C (e.g., 60% of the melting point of VO₂) for their reactive sintering into bulk pellet. Such spark plasma assisted non-equilibrium process brings in the electrical break down process within the sintering that promotes the elementary diffusion and shortens the period associated with the reactive sintering (e.g., 10 minutes). Meanwhile, the residual of the dopant oxides with high melting point within the grain boundary can be used to improve the mechanical properties of the VO₂ pellet. Furthermore, as-proposed SPARS approach makes it possible to flexibly adjust the dopant composition and concentration within VO₂ with high convenience, by just using the powder of pure VO₂ and the dopant oxides as precursors.

3.2. Metal to insulator transition properties for Ti substituted VO₂

As-proposed SPARS approach was first applied to achieve Ti-doping of VO₂, and Fig. 1b shows the X-ray diffraction (XRD) patterns of as-made V_{1-x}Ti_xO₂ pellets. In general, the V_{1-x}Ti_xO₂ exhibit the same crystal structure to VO₂ (M), while their lattice expands with an increasing x as demonstrated in Fig. 1c (see more details of their structure information from the Rietveld refinement in Table S1). It is also worth noticing that the c_0/a_0 in the lattice constant slightly increases indicated by the Rietveld refinements (see Fig. S1), and this observation is in agreement to the understanding by C. N. R. Rao et al that a local structural distortion upon Ti substitution may also relevant to the variation in MIT properties³². This clearly demonstrates the effective substitution of the lattice vanadium within VO₂ by titanium that exhibits larger ionic radius, as is in agreement to the previous report³³. The cross-section morphology of as-sintered V_{1-x}Ti_xO₂ pellet as shown in Fig. 1d demonstrates its polycrystallinity with a grain size of ~20 μm, and the same distribution is observed for V and Ti as further confirmed by the energy dispersion spectroscopy (EDS) shown in Figs. 1e and 1f. **Furthermore, X-ray photoemission spectroscopy (XPS) analysis shown in Fig. 1g indicates the generation of V³⁺ valence state via Ti doping of VO₂, while the valence state of the Ti remains as 4+ as shown in Fig. 1h. The above understanding about the presence of V³⁺ valence state via Ti doping is further confirmed by the XPS results for other Ti-substituted samples, as shown in Figs. S2 and S3. Fig. 1i demonstrates the temperature dependence of resistivity (ρ - T) as measured for as-made V_{1-x}Ti_xO₂ pellets, where abrupt reductions in their resistivity are observed in ρ - T tendencies by elevating temperature across their T_{MIT} . The elevation in the resistivity for the Ti-substituted VO₂ is against the conventional expectation that the presence of V³⁺ should strengthen the metallic phase that reduces the room-temperature resistivity. It is more likely to be associated with the compositing effect of the residual TiO₂ remaining at the grain boundary.**

Nevertheless, this is hard to be distinguished in the XRD or EDS mapping, since the particle size of TiO_2 ($\sim 10\text{-}20$ nm) is much smaller than VO_2 ($\sim 20\text{-}30$ μm) while the crystal structure is also similar for TiO_2 and VO_2 . Similar elevation in the room-temperature resistivity was also previously observed in ref 32, and was attributed to local structure distortion. Therefore, the mechanism related to the Ti doping in VO_2 is expected to be more complicated that is worthy to be further explored in the future. In Fig. 1j, the T_{MIT} of as-made $\text{V}_{1-x}\text{Ti}_x\text{O}_2$ pellets were further plotted as a function of doping concentration. As shown T_{MIT} was the averaged ones from the R - T tendency measured by heating up and cooling down, while each critical temperatures were taken when the temperature coefficient of resistance (TCR) reached the maximum, as illustrated in Fig. S4 and Table S2. It can be seen that as-achieved T_{MIT} exhibits a generally reducing tendency with an increasing substitution concentration of Ti. This observation is in general agreement to the previous report³², and this is attributed to the distorted local structure³² and the presence of V^{3+} valence state induced by the substitution of titanium. We emphasize that the Ti substitution of VO_2 as achieved presently via our SPARS approach reduces the T_{MIT} that is relevant to the Ti doping composition, while the underneath mechanisms could be complicated as is indeed under debate yet according to the previous reports.

3.3. Extending the SPARS strategy to achieved broad regulation in T_{MIT} of VO_2

To further extend the regulation of T_{MIT} , more dopant oxides (e.g., WO_3 , MoO_3 , Nb_2O_5 , Cr_2O_3 and Fe_2O_3) were co-sintered with VO_2 via the as-proposed SPARS approach, and their respective XRD pattern and representative morphology are shown in Fig. S5 and S6, respectively. It can be seen that the as-synthesized polycrystalline ceramic pellets via the spark plasma assisted sintering process exhibit relatively densified morphology without obvious porosity, and this is further confirmed by its pronounced transition abruptness across the T_{MIT} . It can be seen that the as-synthesized polycrystalline doped VO_2 ceramic pellets via the spark plasma assisted sintering process exhibit relatively densified morphology, despite the presence of little amount of pores, as indicated in Fig. S7. The as-observed morphology is in consistency with the previous reports on polycrystalline VO_2 bulk pellets without doping as synthesized by solid-state reaction or spark plasma sintering^{34, 35}. This indicates that the as-proposed SPARS strategy can effectively achieve the reactive sintering process that sinters the precursor powders into densified bulk pellet within largely shortened reaction period of 10 minutes. As their ρ - T tendencies shown in Fig. 2a, the T_{MIT} is more broadly adjusted within 240-350 K. In Fig. 2b, as-achieved T_{MIT} were plotted as a function of the substitution concentration, and further compared with the previous reports^{21, 32, 36-38}. Similar to the previous reports for doped VO_2 samples¹⁹, herein substituting the vanadium with elements at higher valence state (e.g., W^{6+} , Mo^{6+} and Nb^{5+}) reduces the T_{MIT} , while the respective substitution via lower valence elements (e.g., Cr^{3+} and Fe^{3+}) slightly elevates the T_{MIT} . It is worth noticing that apart from the variation in the valence state of vanadium, the variation in the lattice constant owing

to the different ionic radius of the dopants compared to vanadium may also influence the MIT properties. Nevertheless, in the present work, all the dopant elements (e.g., Ti^{4+} , Nb^{5+} , W^{6+} , Mo^{6+} , Cr^{3+} and Fe^{3+}) enlarge the lattice constants of VO_2 as further summarized in the Table S3, but Cr^{3+} and Fe^{3+} increase the T_{MIT} of VO_2 , while Nb^{5+} , W^{6+} and Mo^{6+} reduce its T_{MIT} . This indicates that the regulation in the valence state of vanadium should be a dominant cause to T_{MIT} . In Fig. 2c, the abrupt variations in the resistivity across the MIT ($\rho_{\text{Insul.}} / \rho_{\text{Metal.}}$) is further plotted as a function of T_{MIT} , where the magnitude generally decays with their T_{MIT} . It is in particular worth noticing that high transition abruptness is achieved for Ti substituted VO_2 (e.g., $\rho_{\text{Insul.}} / \rho_{\text{Metal.}}$ exceeding 10^2) that is comparable to the presently commercial critical temperature resistor (CTR) as reported previously³⁹.

To evaluate the ability in regulating the T_{MIT} for various dopant elements, the variation in T_{MIT} is linear fitted with the doping concentration (see Fig. S8), and in Fig. 2d as-obtained slope ($dT_{\text{MIT}} / dn_{\text{dopant}}$) is further plotted as a function of the dopant valence state. It can be seen that the variation in T_{MIT} is more effectively reduced by substituting vanadium with the dopant elements at higher valence states (e.g., -17.9 K \%^{-1} for W^{6+} and -9.4 K \%^{-1} for Nb^{5+}). In contrast, the regulation in T_{MIT} is less effective when the substituting elements exhibits the same or lower valence state compared to V^{4+} (e.g., $+2.6 \text{ K \%}^{-1}$ for Fe^{3+} and -0.43 K \%^{-1} for Ti^{4+}).

3.4. Compliant variation in electronic structures as probed by NEXAFS

To further qualitatively probe the variations in the electronic structures of VO_2 associated with the elementary substitution, the near-edge X-ray absorption fine structure (NEXAFS) analysis was performed, as the results shown in Fig. 3a-3b for V-L edge and O-K edge, respectively. In the V-L spectrum of VO_2 , the V-L_{III} peak ($\sim 518 \text{ eV}$) is recognized to be associated with the $\text{V } 2p_{3/2} \rightarrow 3d$ transition, while the V-L_{II} peak ($\sim 524 \text{ eV}$) reflects the $\text{V } 2p_{1/2} \rightarrow 3d$ transition⁴⁰⁻⁴². From the perspective of the hybridization between V $3d$ and O $2p$ band, the peaks in the O-K edge (e.g., O $1s \rightarrow 2p$ transition) were respectively corresponding to the t_{2g} and e_g orbitals, and the ratio in intensities of t_{2g} / e_g was reported to indicate the orbital occupancy^{43, 44}. Furthermore, the $d_{//}$ orbital associated with the neighboring V ions along the rutile c axis reflects the V-V interaction, while the π^* orbit pointed in the ligands is corresponding to the electron density that is shifted away from the V-O bond direction. In contrast, σ / σ^* orbits with rotational symmetry around V-O bond is associated to the V-O interaction⁴⁵.

Substituting the vanadium with elements at higher valence state (e.g., W^{6+} , Mo^{6+} and Nb^{5+}) results in the leftwards shift of the V-L edge (see Fig. 3a), and this observation is in consistency with the XPS results shown in Fig. S9 (e.g., Fig. S9 a and S9 c) that demonstrate the reduction in the valence state of vanadium towards V^{3+} .

In addition, the as-observed similar peak position of O 1s peak (e.g., ~530.1 eV) for doped VO₂ with respect to the pristine one indicates the main presence of lattice oxygen within the material. Meanwhile, the ratio in intensity of t_{2g}/e_g is observed to be smaller compared to the pristine VO₂, and this demonstrates an enhanced orbital occupancy in t_{2g} band, owing to the electron doping from the higher valence substitution. It is known for VO₂ that electron carrier doping strengthens the metallic phase and reduces T_{MIT} , as illustrated in Fig. 3c²⁰. Therefore, the as-observed reduction in the T_{MIT} via high-valence substitution is associated to the electron occupancy in the t_{2g} band of VO₂. In addition, the as-observed reduced intensity of the t_{2g} peak with respect to the e_g peak also indicates the weakening of direct V-V interactions upon the cationic substitution⁴⁵. It is also interesting to note that similar variations in the electronic structure are observed for Ti substituted VO₂, in which case the V-L edge also shifts leftwards while the t_{2g}/e_g ratio decreases. The above observation is in agreement to the reduction in T_{MIT} for Ti substituted VO₂, although the dopant (Ti⁴⁺) exhibits the same valence state compared to the matrix (V⁴⁺). It is worth noticing that the reduction as observed in the T_{MIT} of Ti doped VO₂ is consistency with the previous reports^{32,46}. Nevertheless, the underneath mechanism associated to the regulation in the T_{MIT} via equivalent substitution is still in debate. For example, C. N. R. Rao *et al* ascribed it to the distorted crystal structure induced by the Ti substitution³², while I. K. Kristensen attributed such result to the variation in carrier concentrations⁴⁶.

In contrast, substituting vanadium with dopant at lower valence state (e.g., Fe³⁺) results in opposite variations in the vanadium valence state, as the V-L edge shifts rightwards in the V-L edge spectrum. This is in agreement to the XPS result that the valence state of vanadium was slightly enhanced towards higher valence (e.g., +5) valence (see Fig. S9 e), and this is also in general consistency to the observed elevation in T_{MIT} , as illustrated in Fig. 3c. Nevertheless, it is worth noticing that the relative intensity of t_{2g} peak, compared to e_g , in the O-K edge is not increased as expected for lower valence element substitution of vanadium, but also reduced. This reveals the presence of a second mechanism that may also influence the electronic structure of the presently made doped VO₂ samples, in addition to the substitution of vanadium. This is most likely to be associated to the generation of oxygen vacancy during the SPARS that will also contribute electron carrier from the perspective of anion regulation⁴⁷, and as a result induce the elevation in T_{MIT} via Fe substitution, as compared to the previous reports³⁸. In addition, the oxygen vacancy within VO₂ is reported to be formed upon a high-temperature vacuum atmosphere, and this is also the case during the SPARS process in coarse vacuum atmosphere⁴⁸. It is also worthy to mention that such potentially generated oxygen vacancy is not the dominate reason for the Ti substitution or higher valence element substitution of vanadium, since a monotonic variation in T_{MIT} with the substitution concentration is indeed observed for all these samples sintered at the same condition. Furthermore, the expected T_{MIT} (around 340 K) and variation in resistivity across MIT (over 10²) similar to the previous reports were achieved in as-sintered VO₂ pellet without any doping, and this

profoundly demonstrate that the potential generation in oxygen vacancy is not problematic in the present work. From the NEXAFS analysis, it is noteworthy that in contrast to conventional semiconductive doping process that mainly alters the carrier concentration, the elementary substitution of VO₂ also results in compliant variation in their electronic structures.

3.5. Meanwhile improving the mechanical strength of the substituted VO₂

Apart from regulating the electronic structures and MIT properties, it is also worth noticing that the mechanical properties of VO₂ pellet can be meanwhile improved along with the elementary substitution process using the SPARS approach via compositing with the residual dopants. Notably, the abrupt variation in the lattice constant of VO₂ across the T_{MIT} is the main problem that interrupts their electronic functionality in potential applications as critical temperature resister (CTR). For example, the structural variation promotes the generation and propagation of the cracks within VO₂ that reduce the abruptness in their MIT and deteriorate the mechanical strength. Therefore, both the MIT properties and the mechanical strength were expected to be improved for the practical electronic applications of VO₂.

Fig. 4a compares the Vickers hardness (H_V) measured for doped VO₂ pellets herein made by SPARS method as a function of the doping concentration. It can be seen that the H_V for doped VO₂ (e.g., over 500 kgf / mm²) largely exceeds the one observed for the pristine VO₂ (e.g., 267.2 kgf / mm²), while H_V shows a generally increasing tendency with the doping concentration. This is attributed to the presence of the residual dopant oxide was not fully diffuse into the lattice of VO₂ during the SPARS process that strengthens the grain boundary. In Fig. 4b, we further summarize the achievable mechanical strength for the doped VO₂ as made in this work plotted as a function of their transition abruptness in resistivity across the T_{MIT} . It clearly demonstrates the feasible type and composition in the dopant oxides to achieve abrupt MIT functionality while maintaining good mechanical strength (marked by the square in Fig. 4b). As-observed mechanical strength in the VO₂ pellet composited with the high melting-point oxides were comparable to the one observed for VO₂ microcrystal as measured by the nanoindentation testing⁴⁹. It is worth noticing that the grain boundary within polycrystalline VO₂ bulk material inevitably leads to the suppression in its macro mechanical property, as compared with the nanoindentation associated to the nanoscale hardness.

In particular, the co-sintering of VO₂ with dopant oxides exhibiting high melting point (e.g., Al₂O₃, HfO₂ and CoO) not only improve the mechanical strength of the pellets, but also enhance the transition abruptness in their ρ - T tendencies across T_{MIT} . This is demonstrated in Fig. 4c, where more abrupt MIT functionality with similar T_{MIT} is observed for Hf, Al and Co doped VO₂ pellet compared to the pristine VO₂ pellet. In particular, the magnitude of their basic resistivity at room-temperature (ρ_{300K}) can be regulated within a broad range across two orders of magnitudes as

demonstrated in Fig. 4d, and this is expected to extend the thermistor functionality. As a representative, Fig. 4e demonstrates the distribution of the elementary distribution of V, Co and O as measured by energy dispersion spectroscopy (EDS) for co-sintered VO₂ and CoO with a nominal composition of V_{0.7}Co_{0.3}O₂. It can be seen that the cobalt element is not observed in the region associated with the vanadium dioxides, and this differs to the situation for the aforementioned dopant oxides with low melting points (e.g., WO₃, Nb₂O₅, TiO₂, etc.).

The above results indicate the less effective diffusion of Co within VO₂ during the sintering process owing to the relatively high melting point of CoO (see more details in Fig. S10), and this is in agreement to the small variation in T_{MIT} as observed in Fig. S11. This understanding is further confirmed by the Rietveld refinement of their XRD patterns as shown in Fig. S12, while their corresponding percentage of residual dopants (e.g., Al₂O₃, CoO, Nb₂O₅, WO₃ and TiO₂) were further summarized in Table S4. It demonstrates that the reaction ratio (P_{react}) between the dopant oxides with low melting point (T_{melt}) and VO₂ (e.g., P_{react} is of almost ~ 99.6 % for Nb₂O₅ with T_{melt} of 1485 °C) largely exceeds the ones observed for the dopant oxides with high T_{melt} (e.g., P_{react} is of ~ 80 % for CoO with T_{melt} for 1935 °C). Nevertheless, the residual dopant oxides, such as Al₂O₃, HfO₂ and CoO, significantly improve the mechanical properties of VO₂ without sacrificing the MIT properties. **From the perspective of mechanical properties, the presence of compositing oxides at high insulating state (e.g., Al₂O₃, HfO₂ and Co₃O₄) can effectively prohibit the generation and propagation of the cracks along the grain boundary. Therefore, a more stable electronic functionality for the as-made doped VO₂ bulk material is expected, which is a critical issue for the practical applications in electronic devices upon thermoshock. From the perspective of MIT properties, the compositing with the insulating oxides located at the grain boundary can reduce the charge leakage along the cracks within grain boundary for the insulating phase of VO₂, and this leads to abrupt transitions in resistivity across the T_{MIT} . Similar effects were also previously reported for the vanadium phosphate glass (VPG)⁵⁰ and vanadium-based critical temperature resistor³⁹. Therefore, a more stable electronic functionality for the as-made doped VO₂ bulk material is expected, which is a critical issue for the practical applications in electronic devices upon thermoshock⁵¹.**

4. Conclusions

In summary, we largely improved the effectiveness in regulating the MIT functionality via elementary doping as well as the mechanical properties of VO₂ bulk material by developing a spark plasma assisted reactive sintering (SPARS) approach. Compared to the conventional solid-state reactions, the spark plasma induced non-equilibrium process promotes the diffusion of the dopant element from its oxide precursor into the lattice of the powder of VO₂ within a largely shortened co-sintering period of ~10 minutes. This brings in high flexibility and convenience to control the dopant type and concentration within bulk VO₂, enabling a broad adjustment in the

T_{MIT} (e.g., within 240-350 K). In contrast to conventional semiconductive doping process, compliant variations in the electronic structure are observed within the doped VO_2 as probed by NEXAFS, and therefore variation in the MIT properties is more likely to be associated with the doping-induced electronic orbital regulation rather than simply varying the carrier concentration. Furthermore, the mechanical strength of the doped VO_2 bulk material can be meanwhile largely improved (e.g., from 267.2 to 950 kgf / mm²), owing to compositing effect of the unreacted high melting-point oxides. The high tunability in the MIT functionality and improved mechanical strength as enabled by the SPARS approach pave the way towards practical applications of VO_2 as a bulk material in power electronics.

Notes

The authors declare no competing financial interest.

Acknowledgements

This work was supported by the National Key Research and Development Program of China (No. 2021YFA0718900), the National Natural Science Foundation of China (No. 62074014 and 52073090), and the Beijing New-star Plan of Science and Technology (No. Z191100001119071).

Supporting Information

Supporting information is available online. See the supporting information for more details about the synthesis method, the derivation of T_{MIT} , X-ray diffraction (XRD) patterns, the energy dispersion spectrum (EDS), X-ray photoelectron spectroscopy (XPS), the Rietveld refinements and additional analysis results.

Correspondences: Correspondences should be addressed: Prof. Jikun Chen (jikunchen@ustb.edu.cn), Prof. Yong Jiang (yjiang@ustb.edu.cn) and Prof. Nuofu Chen (nfchen@ncepu.edu.cn).

References

- (1) Ke, Y.; Zhang, B.; Wang, T.; Zhong, Y.; Vu, T. D.; Wang, S.; Liu, Y.; Magdassi, S.; Ye, X.; Zhao, D.; et al. Manipulating atomic defects in plasmonic vanadium dioxide for superior solar and thermal management. *Mater. Horiz.* **2021**, *8* (6), 1700-1710.
- (2) Morrison, V. R.; Chatelain, R. P.; Tiwari, K. L.; Hendaoui, A.; Bruhacs, A.; Chaker, M.; Siwick, B. J. A photoinduced metal-like phase of monoclinic VO₂ revealed by ultrafast electron diffraction. *Science* **2014**, *346* (6208), 445-448.
- (3) Zhou, X.; Li, H.; Meng, F.; Mao, W.; Wang, J.; Jiang, Y.; Fukutani, K.; Wilde, M.; Fugetsu, B.; Sakata, I.; et al. Revealing the Role of Hydrogen in Electron-Doping Mottronics for Strongly Correlated Vanadium Dioxide. *J. Phys. Chem. Lett.* **2022**, *13* (34), 8078-8085.
- (4) Tang, K.; Dong, K.; Li, J.; Gordon, M. P.; Reichertz, F. G.; Kim, H.; Rho, Y.; Wang, Q.; Lin, C.-Y.; Grigoropoulos, C. P.; et al. Temperature-adaptive radiative coating for all-season household thermal regulation. *Science* **2021**, *374* (6574), 1504-+.
- (5) Wang, S.; Jiang, T.; Meng, Y.; Yang, R.; Tan, G.; Long, Y. Scalable thermochromic smart windows with passive radiative cooling regulation. *Science* **2021**, *374* (6574), 1501-+.
- (6) Cui, Y.; Ke, Y.; Liu, C.; Chen, Z.; Wang, N.; Zhang, L.; Zhou, Y.; Wang, S.; Gao, Y.; Long, Y. Thermochromic VO₂ for Energy-Efficient Smart Windows. *Joule* **2018**, *2* (9), 1707-1746.
- (7) Kats, M. A.; Blanchard, R.; Zhang, S.; Genevet, P.; Ko, C.; Ramanathan, S.; Capasso, F. Vanadium Dioxide as a Natural Disordered Metamaterial: Perfect Thermal Emission and Large Broadband Negative Differential Thermal Emittance. *Phys. Rev. X* **2013**, *3* (4).
- (8) Tang, K.; Wang, X.; Dong, K.; Li, Y.; Li, J.; Sun, B.; Zhang, X.; Dames, C.; Qiu, C.; Yao, J.; et al. A Thermal Radiation Modulation Platform by Emissivity Engineering with Graded Metal-Insulator Transition. *Adv. Mater.* **2020**, *32* (36).
- (9) Zhang, H.-T.; Park, T. J.; Islam, A. N. M. N.; Tran, D. S. J.; Manna, S.; Wang, Q.; Mondal, S.; Yu, H.; Banik, S.; Cheng, S.; et al. Reconfigurable perovskite nickelate electronics for artificial intelligence. *Science (New York, N.Y.)* **2022**, *375* (6580), 533-539.
- (10) Zhang, H.-T.; Park, T. J.; Zaluzhnyy, I. A.; Wang, Q.; Wadekar, S. N.; Manna, S.; Andrawis, R.; Sprau, P. O.; Sun, Y.; Zhang, Z.; et al. Perovskite neural trees. *Nat. Commun.* **2020**, *11* (1).
- (11) Zhang, Z.; Mondal, S.; Mandal, S.; Allred, J. M.; Aghamiri, N. A.; Fali, A.; Zhang, Z.; Zhou, H.; Cao, H.; Rodolakis, F.; et al. Neuromorphic learning with Mott insulator NiO. *PNAS* **2021**, *118* (39).
- (12) Chen, J.; Hu, H.; Wang, J.; Yajima, T.; Ge, B.; Ke, X.; Dong, H.; Jiang, Y.; Chen, N. Overcoming synthetic metastabilities and revealing metal-to-insulator transition & thermistor bi-functionalities for d-band correlation perovskite nickelates. *Mater. Horiz.* **2019**, *6* (4), 788-795.
- (13) Park, J. H.; Coy, J. M.; Kasirga, T. S.; Huang, C.; Fei, Z.; Hunter, S.; Cobden, D. H. Measurement of a solid-state triple point at the metal-insulator transition in VO₂. *Nature* **2013**, *500* (7463), 431-434.
- (14) Jeong, J.; Aetukuri, N.; Graf, T.; Schladt, T. D.; Samant, M. G.; Parkin, S. S. P. Suppression of Metal-Insulator Transition in VO₂ by Electric Field-Induced Oxygen Vacancy Formation. *Science* **2013**, *339* (6126), 1402-1405.
- (15) Lee, D.; Chung, B.; Shi, Y.; Kim, G. Y.; Campbell, N.; Xue, F.; Song, K.; Choi, S. Y.; Podkaminer, J. P.; Kim, T. H.; et al. Isostructural metal-insulator transition in VO₂. *Science* **2018**, *362* (6418), 1037-+.
- (16) Zhou, X.; Wu, Y.; Yan, F.; Zhang, T.; Ke, X.; Meng, K.; Xu, X.; Li, Z.; Miao, J.; Chen, J.; et al. Revealing the high sensitivity in the metal toinsulator transition properties of the pulsed laser deposited VO₂ thin films. *Ceram. Int.* **2021**, *47* (18), 25574-25579.

- (17) Janod, E.; Tranchant, J.; Corraze, B.; Querre, M.; Stoliar, P.; Rozenberg, M.; Cren, T.; Roditchev, D.; Vinh Ta, P.; Besland, M.-P.; et al. Resistive Switching in Mott Insulators and Correlated Systems. *Adv. Funct. Mater.* **2015**, *25* (40), 6287-6305.
- (18) Liu, K.; Lee, S.; Yang, S.; Delaire, O.; Wu, J. Recent progresses on physics and applications of vanadium dioxide. *Mater. Today* **2018**, *21* (8), 875-896.
- (19) Shibuya, K.; Kawasaki, M.; Tokura, Y. Metal-insulator transition in epitaxial $V_{1-x}W_xO_2$ ($0 \leq x \leq 0.33$) thin films. *Appl. Phys. Lett.* **2010**, *96* (2).
- (20) Sakai, E.; Yoshimatsu, K.; Shibuya, K.; Kumigashira, H.; Ikenaga, E.; Kawasaki, M.; Tokura, Y.; Oshima, M. Competition between instabilities of Peierls transition and Mott transition in W-doped VO_2 thin films. *Phys. Rev. B* **2011**, *84* (19).
- (21) Takami, H.; Kanki, T.; Ueda, S.; Kobayashi, K.; Tanaka, H. Filling-controlled Mott transition in W-doped VO_2 . *Phys. Rev. B* **2012**, *85* (20).
- (22) Holman, K. L.; McQueen, T. M.; Williams, A. J.; Klimczuk, T.; Stephens, P. W.; Zandbergen, H. W.; Xu, Q.; Ronning, F.; Cava, R. J. Insulator to correlated metal transition in $V_{1-x}Mo_xO_2$. *Phys. Rev. B* **2009**, *79* (24).
- (23) Soltani, M.; Chaker, M.; Haddad, E.; Kruzelecky, R. V.; Margot, J. Effects of Ti-W codoping on the optical and electrical switching of vanadium dioxide thin films grown by a reactive pulsed laser deposition. *Appl. Phys. Lett.* **2004**, *85* (11), 1958-1960.
- (24) Goncalves, A.; Resende, J.; Marques, A. C.; Pinto, J. V.; Nunes, D.; Marie, A.; Goncalves, R.; Pereira, L.; Martins, R.; Fortunato, E. Smart optically active VO_2 nanostructured layers applied in roof-type ceramic tiles for energy efficiency. *Sol. Energy Mater. Sol. Cells* **2016**, *150*, 1-9.
- (25) Wu, Y.; Fan, L.; Liu, Q.; Chen, S.; Huang, W.; Chen, F.; Liao, G.; Zou, C.; Wu, Z. Decoupling the Lattice Distortion and Charge Doping Effects on the Phase Transition Behavior of VO_2 by Titanium (Ti^{4+}) Doping. *Sci. Rep.* **2015**, *5*.
- (26) Foltyn, S. R.; Civale, L.; Macmanus-Driscoll, J. L.; Jia, Q. X.; Maiorov, B.; Wang, H.; Maley, M. Materials science challenges for high-temperature superconducting wire. *Nat. Mater.* **2007**, *6* (9), 631-642.
- (27) Florea, M.; Avram, D.; Maraloiu, V. A.; Cojocaru, B.; Tiseanu, C. Heavy doping of ceria by wet impregnation: a viable alternative to bulk doping approaches. *Nanoscale* **2018**, *10* (37), 18043-18054.
- (28) Silversmit, G.; Depla, D.; Poelman, H.; Marin, G. B.; De Gryse, R. Determination of the V 2p XPS binding energies for different vanadium oxidation states (V^{5+} to V^{0+}). *J. Electron Spectrosc. and Related Phenomena* **2004**, *135* (2-3), 167-175.
- (29) Lee, D.; Kim, H.; Kim, J. W.; Lee, I. J.; Kim, Y.; Yun, H.-J.; Lee, J.; Park, S. Hydrogen incorporation induced the octahedral symmetry variation in VO_2 films. *Appl. Surf. Sci.* **2017**, *396*, 36-40.
- (30) Su, X.; Fu, F.; Yan, Y.; Zheng, G.; Liang, T.; Zhang, Q.; Cheng, X.; Yang, D.; Chi, H.; Tang, X.; et al. Self-propagating high-temperature synthesis for compound thermoelectrics and new criterion for combustion processing. *Nat. Commun.* **2014**, *5*.
- (31) Yang, D.; Su, X.; Li, J.; Bai, H.; Wang, S.; Li, Z.; Tang, H.; Tang, K.; Luo, T.; Yan, Y.; et al. Blocking Ion Migration Stabilizes the High Thermoelectric Performance in Cu_2Se Composites. *Adv. Mater.* **2020**, *32* (40).
- (32) Rao, C. N. R.; Natarajan, M.; Subba Rao, G. V.; Loehman, R. E. Phase transitions and conductivity anomalies in solid solutions of VO_2 with TiO_2 , NbO_2 , and MoO_2 . *J. Phys. Chem. Solids*

1971, 32 (6), 1147-1150.

(33) Chen, S.; Liu, J.; Wang, L.; Luo, H.; Gao, Y. Unraveling Mechanism on Reducing Thermal Hysteresis Width of VO₂ by Ti Doping: A Joint Experimental and Theoretical Study. *J. Phys. Chem. C* **2014**, *118* (33), 18938-18944.

(34) Kato, K.; Lee, J.; Fujita, A.; Shirai, T.; Kinemuchi, Y. Influence of strain on latent heat of VO₂ ceramics. *J. Alloy. Compd.* **2018**, *751*, 241-246.

(35) Victor, J.-L.; Gaudon, M.; Penin, N.; Chiron, A.; Chung, U. C.; Viraphong, O.; Rougier, A. Innovative sintering process for fabrication of thermochromic smooth VO₂ ceramics. *J. Alloy. Compd.* **2022**, *890*, 161890.

(36) Wang, Z.-L.; Zhang, R.; Chen, X.-H.; Fu, Q.-S.; Li, C.-L.; Yuan, S.-L.; Zhao, X.-J.; Tao, H.-Z. Nb doping effect in VO₂ studied by investigations of magnetic behavior. *Ceram. Int.* **2018**, *44* (7), 8623-8627.

(37) Liu, S.-J.; Fang, H.-W.; Su, Y.-T.; Hsieh, J.-H. Metal-insulator transition characteristics of Mo- and Mn-doped VO₂ films fabricated by magnetron cosputtering technique. *J. J. Appl. Phys.* **2014**, *53* (6).

(38) Victor, J.-L.; Gaudon, M.; Salvatori, G.; Toulemonde, O.; Penin, N.; Rougier, A. Doubling of the Phase Transition Temperature of VO₂ by Fe Doping. *J. Phys. Chem. Lett.* **2021**, *12* (32), 7792-7796.

(39) Futaki, H. A New Type Semiconductor (Critical Temperature Resistor). *J. J. Appl. Phys.* **1965**, *4* (1), 28-41.

(40) Aetukuri, N. B.; Gray, A. X.; Drouard, M.; Cossale, M.; Gao, L.; Reid, A. H.; Kukreja, R.; Ohldag, H.; Jenkins, C. A.; Arenholz, E.; et al. Control of the metal-insulator transition in vanadium dioxide by modifying orbital occupancy. *Nat. Phys.* **2013**, *9* (10), 661-666.

(41) Wei, J.; Ji, H.; Guo, W.; Nevidomskyy, A. H.; Natelson, D. Hydrogen stabilization of metallic vanadium dioxide in single-crystal nanobeams. *Nat. Nanotechnol.* **2012**, *7* (6), 357-362.

(42) Phu Tran Phong, L.; Hofhuis, K.; Rana, A.; Huijben, M.; Hilgenkamp, H.; Rijnders, G. A. J. H. M.; ten Elshof, J. E.; Koster, G.; Gauquelin, N.; Lumbbeck, G.; et al. Tailoring Vanadium Dioxide Film Orientation Using Nanosheets: a Combined Microscopy, Diffraction, Transport, and Soft X-Ray in Transmission Study. *Adv. Funct. Mater.* **2020**, *30* (1).

(43) Yoon, H.; Choi, M.; Lim, T.-W.; Kwon, H.; Ihm, K.; Kim, J. K.; Choi, S.-Y.; Son, J. Reversible phase modulation and hydrogen storage in multivalent VO₂ epitaxial thin films. *Nat. Mater.* **2016**, *15* (10), 1113-+.

(44) Chen, Y.; Wang, Z.; Chen, S.; Ren, H.; Wang, L.; Zhang, G.; Lu, Y.; Jiang, J.; Zou, C.; Luo, Y. Non-catalytic hydrogenation of VO₂ in acid solution. *Nat. Commun.* **2018**, *9*.

(45) Ruzmetov, D.; Senanayake, S. D.; Narayanamurti, V.; Ramanathan, S. Correlation between metal-insulator transition characteristics and electronic structure changes in vanadium oxide thin films. *Phys. Rev. B* **2008**, *77* (19).

(46) Kristensen, I. K. Semiconductor-to-Semiconductor Transition in the Pseudobinary System TiO₂-VO₂. *J. Appl. Phys.* **1968**, *39* (11), 5341-5342.

(47) Zhang, W.; Wang, K.; Fan, L.; Liu, L.; Guo, P.; Zou, C.; Wang, J.; Qian, H.; Ibrahim, K.; Yan, W.; et al. Hole Carriers Doping Effect on the Metal-Insulator Transition of N-Incorporated Vanadium Dioxide Thin Films. *J. Phys. Chem. C* **2014**, *118* (24), 12837-12844.

(48) Zhang, Z.; Zuo, F.; Wan, C.; Dutta, A.; Kim, J.; Rensberg, J.; Nawrodt, R.; Park, H. H.; Larrabee, T. J.; Guan, X.; et al. Evolution of Metallicity in Vanadium Dioxide by Creation of Oxygen Vacancies. *Phys. Rev. Appl.* **2017**, *7* (3), 034008.

- (49) Verma, D.; Singh, D.; Balakrishnan, V. Fracture toughness of VO₂ microcrystals across metal-insulator transition. *Mater. Lett.* **2022**, 315.
- (50) Iyon, A. I.; Kolbunov, V. R.; Chernenko, I. M. Conductivity stabilization by metal and oxide additives in ceramics on the basis of VO₂ and glass V₂O₅-P₂O₅. *J. Non Cryst. Solids* **2005**, 351 (46), 3649-3654.
- (51) Iyon, A. I.; Kolbunov, V. R.; Chernenko, I. M. Stability of electrical properties of vanadium dioxide based ceramics. *J. Eur. Ceram. Soc.* **1999**, 19 (10), 1883-1888.

Figures and captions

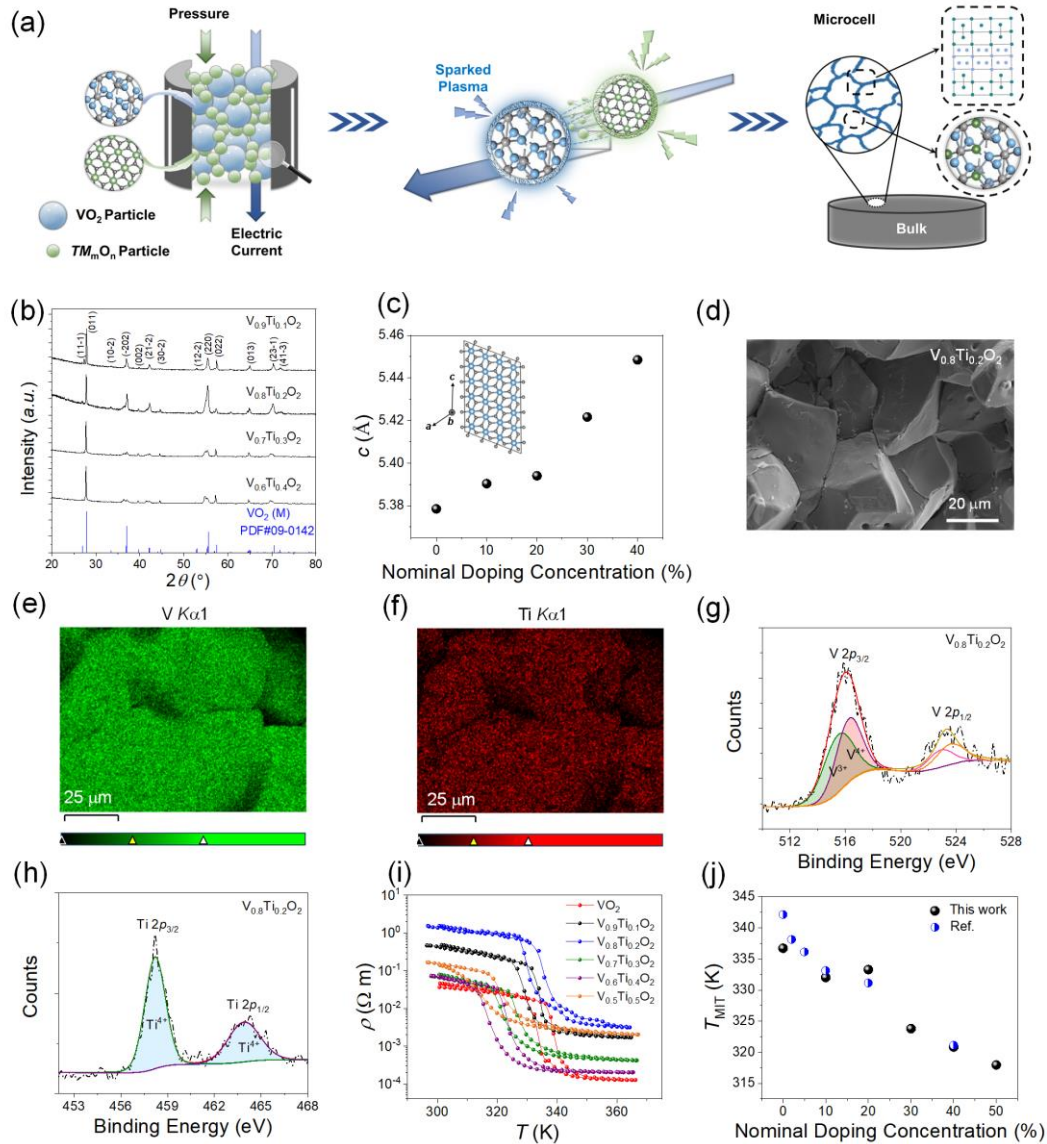


Fig. 1. (a) Schematic illustration of as-proposed spark plasma assisted reactive sintering (SPARS) doping strategy that achieves the elementary doping and grain boundary modifications of the bulk VO_2 . (b) X-ray diffraction (XRD) patterns of as-made $\text{V}_{1-x}\text{Ti}_x\text{O}_2$ bulk material (x from 0.1 to 0.4), as indexed to the structure of the VO_2 (M) with the $P2_1/c$ space group. (c) The c -axis lattice constants of as-made $\text{V}_{1-x}\text{Ti}_x\text{O}_2$ plotted as a function of x. (d) The cross-section surface morphology of as-synthesized $\text{V}_{0.8}\text{Ti}_{0.2}\text{O}_2$ bulk material from scanning electron microscopy (SEM). (e), (f) The energy dispersion spectrum (EDS) of (e) V and (f) Ti elements for the as-made $\text{V}_{0.8}\text{Ti}_{0.2}\text{O}_2$ bulk. (g), (h) The X-ray photoemission spectroscopy (XPS) analysis of (g) V 2p peak and (h) O 1s peak for the $\text{V}_{0.8}\text{Ti}_{0.2}\text{O}_2$ bulk. (i) Temperature dependence of the resistivity for as-made $\text{V}_{1-x}\text{Ti}_x\text{O}_2$. (j) The metal to insulator transition temperature (T_{MIT}) of as-made $\text{V}_{1-x}\text{Ti}_x\text{O}_2$ plotted as a function of the nominal Ti substitution concentration, compared with the previous report³².

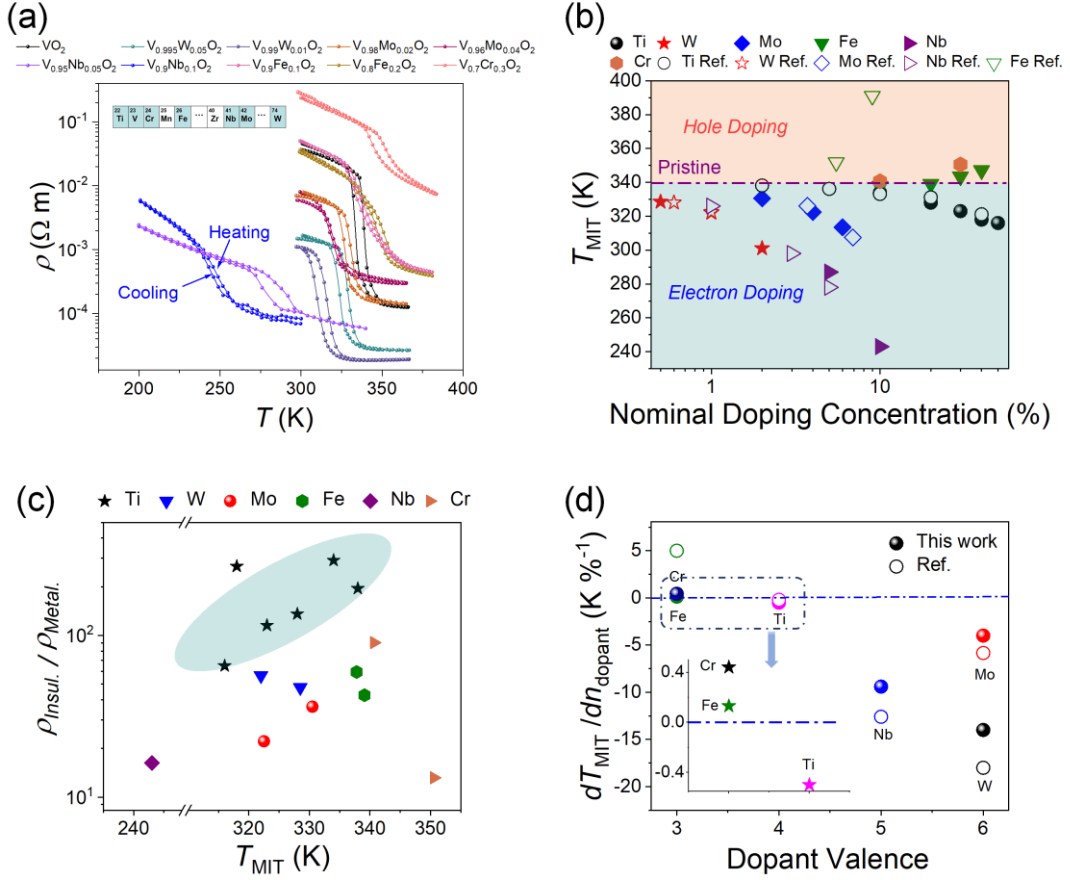


Fig. 2. (a) The temperature dependence of the resistivity for as-made transitional metal (*TM*) doped VO₂ pellet (*TM* = Fe, W, Nb, Cr and Mo). (b) The T_{MIT} of as-made doped VO₂ plotted as a function of the nominal doping concentration and also compared to the previous reports^{19, 22, 32, 36, 38}. (c) The variation in the resistivity across the metal to insulator transition ($\rho_{Insul.} / \rho_{Metal.}$) of the doped VO₂ made in this work, plotted as a function of their metal to insulator transition temperature (T_{MIT}). (d) The modulation capability in T_{MIT} , as evaluated by dT_{MIT} / dn_{dopant} , for various *TM* dopant elements plotted as a function of their valence state, as also compared with the previous reports^{19, 22, 32, 36, 38}. The inset shows the zoom in results for Ti, Cr and Fe.

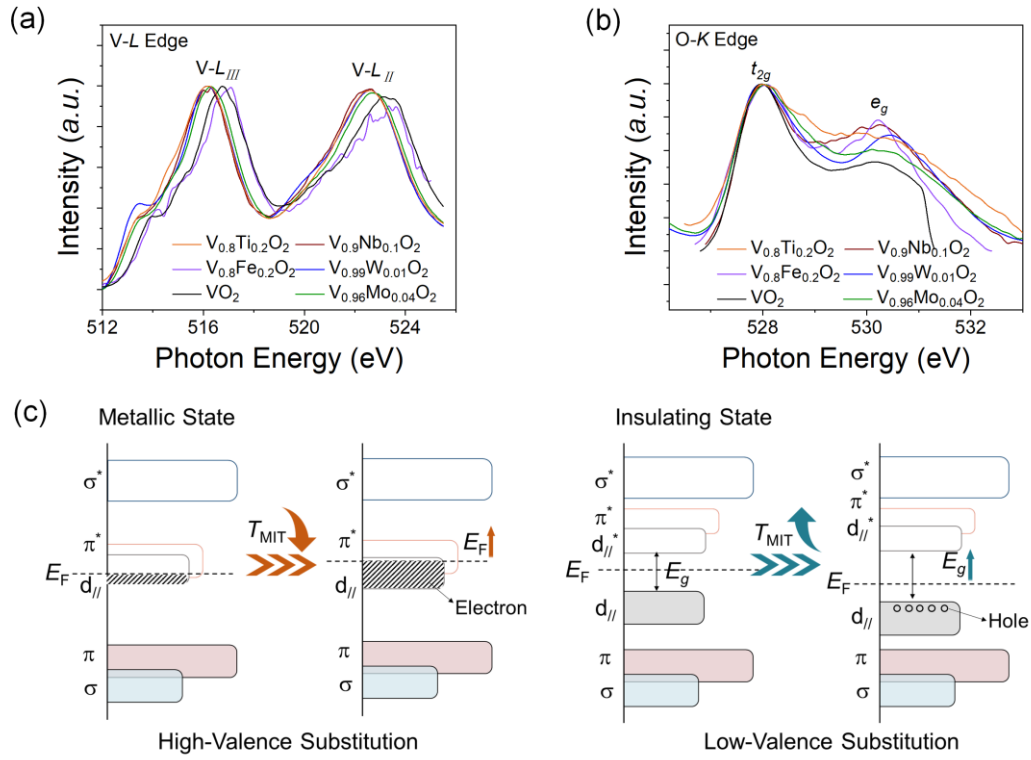


Fig. 3. (a), (b) The near-edge X-ray absorption fine structure (NEXAFS) analysis of (a) V-L edge and (b) O-K edge for the transitional metal (*TM*) substituted VO₂ (*TM* = Ti, Fe, W, Nb and Mo), compared to the pristine VO₂. (c) Illustrating the variation in electronic structures of VO₂ via high-valence (e.g., W, Nb and Mo) and low-valence (e.g., Fe and Cr) *TM* substitutions.

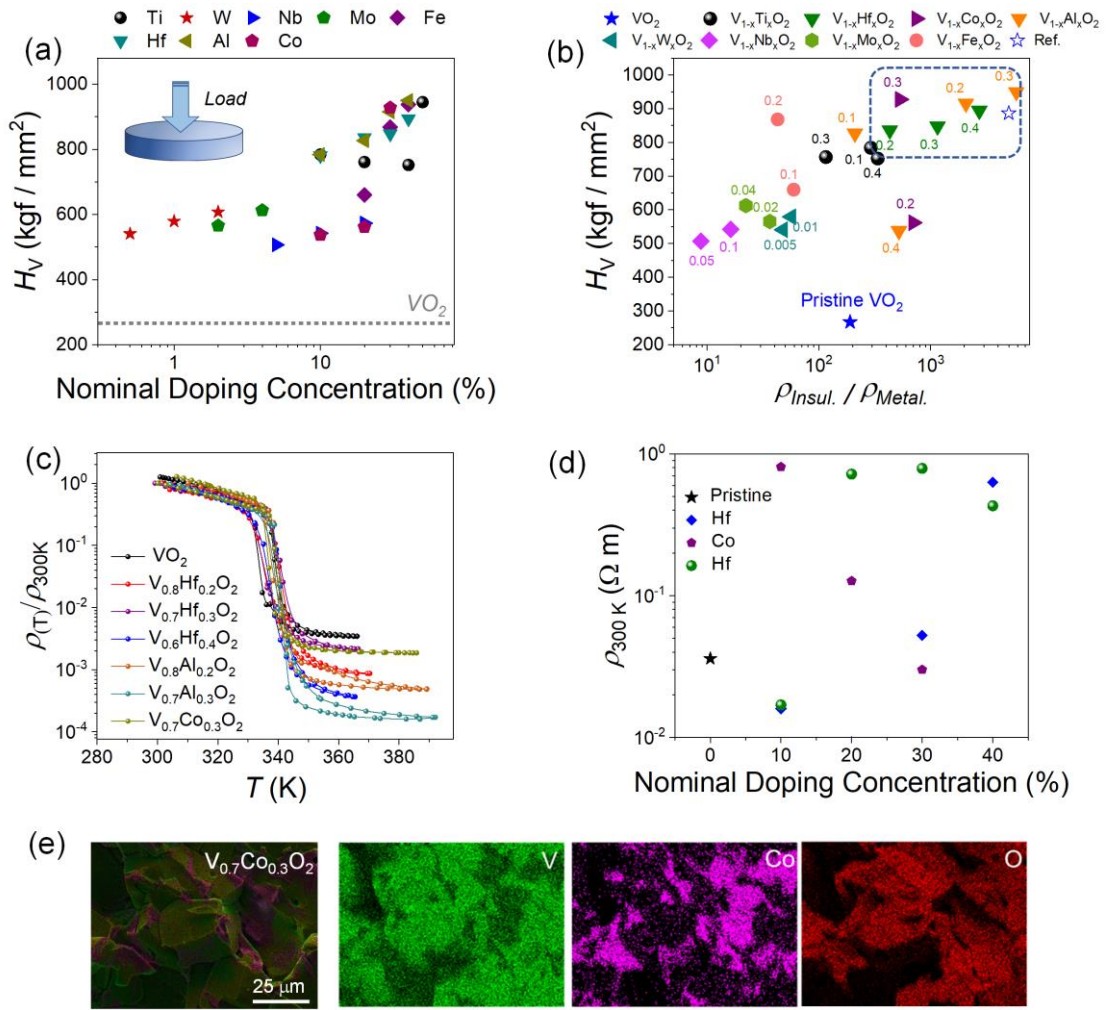


Fig. 4. (a) The Vickers hardness (H_V) for the transitional metal (TM) substituted VO_2 (TM = Ti, Fe, W, Nb, Mo, Hf, Al and Co) made herein, plotted as a function of the nominal doping concentration. (b) Plotting H_V as a function of the variation in resistivity across the metal to insulator transition temperature (e.g., $\rho_{Insul.} / \rho_{Metal.}$) for as-made $V_{1-x}TM_xO_2$ (the number of x is marked near the data points) pellet, as compared with the ref. 45. (c) The normalized temperature dependence of the resistivity ($\rho-T$) of the co-sintered VO_2 with transitional metal oxides with high melting points. (d) The basic resistivity at room-temperature of as-made $V_{1-x}TM_xO_2$ plotted as a function of the nominal doping concentration. (e) The energy dispersion spectrum (EDS) of V, Co and O elements for the as-made $V_{0.7}Co_{0.3}O_2$ pellet.